Reduction of the occupational radiation dose of hybrid operating theater staff during peripheral endovascular procedures

Submitted in partial fulfillment of the requirements for the degree of

Master of Science

Medical Imaging and Interventions

University of Twente

by

ARJAN KOSTER

March 2018

Chairman and Technological supervisor:	Prof. Dr. Ir. C.H. Slump
Medical supervisor:	Dr. C.E.V. Hazenberg
Mentor:	Dr. M. Groenier
Daily supervisor:	MSc. M.M. Jansen

UNIVERSITY OF TWENTE.

UMC Utrecht

ACKNOWLEDGEMENT

This thesis is the culmination of more than a year's work at the department of vascular surgery of the University Medical Center in Utrecht. I would like to thank the endovascular intervention team for their collaboration, collegiality and support. This research would not have been possible without their help. I would like to specifically thank my supervisors Stijn Hazenberg, Kees Slump, Marleen Groenier and Marloes Jansen. Stijn, who provided me with invaluable clinical insights on my research and gave me rational advice when needed. Kees, who helped me get a grasp on complex technical concepts. Marleen, who helped me during the toughest times and was always there to ask the right provocative questions and made me learn more about myself. Marloes, who provided me with a wealth of information about the hybrid operating theater, radiation hygiene and statistical analysis. She was never more than two doors away to listen to my endless questions.

Place: Utrecht

Date: 01/03/2018 **Arjan Koster**

TABLE OF CONTENTS

ACKNOWLEDGEMENT i
LIST OF FIGURES iv
LIST OF TABLES vi
LIST OF TERMS AND ABBREVIATIONS vi

List of Terms and Abbreviations **vii**

1 General introduction **1**
1.1 Thesis outline 1
1.2 Clinical and Technical background 2
1.2.1 Peripheral arterial disease 2
1.2.2 treatment options 3
1.2.3 Fluoroscopic imaging and the Hybrid operating theater 4
1.2.4 Scattered radiation 5

2 Reduction of scatter-induced operator dose by means of a radiation absorbing sterile drape **7**
2.1 Abstract 7
2.2 Introduction 7
2.3 Materials and methods 8
2.3.1 Patients 8
2.3.2 Radiation shielding 8
2.3.3 Dosimetry 9
2.3.4 Statistical analysis 10
2.4 Results 11
2.5 Discussion 14
2.6 Conclusion 15

3 Assessing the feasibility of dual-energy fluoroscopy images in creating calcium and iodine thickness maps **16**

3.1 Abstract 16

3.2 Introduction 16

3.3 Materials and methods 17

3.3.1 Imaging system and protocols 17

3.3.2 Cadaver experiment 18

3.3.3 Basic material decomposition 18

3.4 Results 20

3.5 Discussion 21

3.6 Conclusion 22

REFERENCES 23

Appendix A Dosimetry study **28**

LIST OF FIGURES

1.1 **(a)** Percutaneous balloon angioplasty **(b)** Balloon-expandable stenting. . 3

1.2 The ceiling mounted Philips Allura Xper FD20 Flexmove fluoroscopy system. 4

1.3 **(a)** Digital Subtraction Angiography (DSA) image without contrast in the popliteal artery. The arterial lumen is not visible. **(b)** DSA image with intravenous contrast agent, allowing the popliteal artery to be distinguished from surrounding tissues. 5

1.4 Compton interactions between the primary x-ray beam of the imaging system and the patient produce scattered radiation. This radiation is the primary contributor to the occupational dose of hybrid operating theater personnel. 6

2.1 **(a)** Example of possible FO and SO positions during endovascular intervention at the femoral level. **(b)** Example of ceiling screen (asterisks) and RADPAD (arrows) placement. 9

2.2 Cumulative DAP-adjusted operator doses for the control group (n=24) and study group (n=25): **(a)** DSA runs, **(b)** fluoroscopy runs, **(c)** total dataset. 13

2.3 Cumulative uncompensated operator doses for the control group (n=24) and study group (n=25): **(a)** DSA runs, **(b)** fluoroscopy runs, **(c)** total dataset. 13

3.1 Frontal views of the femoral section of a cadaveric leg. Included in the images is part of the femur as well as a calcified femoral artery, filled with contrast agent. **(a)** 80 KvP image **(b)** 120 KvP image **(c)** Calcium thickness map **(d)** Iodine thickness map 20

3.2 Thickness maps created using E_eff values of 80 and 50 KeV for the 120 and 80 kV anode voltage pictures, respectively. **(a)** Calcium thickness map **(b)** Iodine thickness map 21

A.1 Residuals plots for the *per-run* fluoroscopy data subset. **Left:** Residual plot; the two lines correspond with the control and study groups **Right:** Distribution of residuals 29

A.2 Residuals plots for the *per-run* DSA data subset. **Left:** Residual plot; the two lines correspond with the control and study groups **Right:** Distribution of residuals 29

A.3 Residuals plots for the *per-run* total dataset. **Left:** Residual plot; the two lines correspond with the control and study groupst **Right:** Distribution of residuals 30

A.4 Scatterplot of the measured operator dose on the y-axis versus the DAP of the associated imaging run on the x-axis. The regression line was fitted using a linear regresssion model which showed an R-squared value of 0.36 30

LIST OF TABLES

1.1 Fontaine classification 2
1.2 Ankle-brachial index 2
2.1 Patient characteristics and procedure details 11
2.2 Procedure locations and RADPADs used 11
2.3 Likelihood ratio tests 12
2.4 Multivariate analysis of *Dose per run* data 12

List of Terms and Abbreviations

FO First Operator

SO Second Operator

SN Sterile Nurse

NSN Non-sterile Nurse

AN Anesthesiologist

OR Operating Room

PAD Peripheral Arterial Disease

CLI Critical Limb Ischaemia

CI Claudicatio Intermittens

ABI Ankle-Brachial Index

PTA Percutaneous Transluminal Angioplasty

DCB Drug-coated Balloon

PDM Personal Dosimeter

DAP Dose Area Product

kVp Kilovolt Peak

mAs Milliampre-second

FT Fluoroscopy Time

AK Air Kerma

AIC Arteria Iliaca Communis

AII Arteria Iliaca Interna

AIE Arteria Iliaca Externa

AFC Arteria Femoralis Communis

AFP Arteria Femoralis Profunda

AFS Arteria Femoralis Superficialis

BMI Body Mass Index

EPR Electronic Patient Record

DSA Digital Subtraction Angiography

IRCP International Commission on Radiological Protection

ALARA As Low As Reasonably Achievable

BMD Basic Material Decomposition

SNR Signal-to-Noise Ratio

GDL Gemeenschappelijk Dierenlaboratorium

CHAPTER 1

General introduction

1.1 Thesis outline

The aim of this thesis is to explore two different approaches to reducing the occupational radiation exposure in the hybrid operating theater. Each approach will be described in a different chapter. since these chapters will not contain extensive background information on endovascular interventions, chapter one is reserved for this purpose.

Chapter two contains a prospective study aimed at evaluating the occupational radiation dose for operating theater personnel caused by scattered radiation from the patient, as a consequence of fluoroscopic imaging during endovascular interventions. The efficacy of a radiation absorbing sterile drape is assessed with the ultimate goal of reducing the occupational radiation dose of hybrid operating theater personnel.

Research question: *Does the use of a radiation absorbing sterile drape significantly reduce scattered radiation dose for operating theater personnel during peripheral endovascular procecures?*

Chapter three contains a cadaver experiment undertaken in order to assess the feasibility of creating dual-energy imaging projections through a basic material decomposition algorithm by using dual-energy fluoroscopy images created using a c-arm x-ray system. The ultimate goal is to reduce the imaging time during peripheral endovascular procedures in the hybrid operating theater by providing the surgeon with additional information regarding calcified lesions, thereby reducing the occupational radiation dose.

Research question: *Is the use of dual-energy fluoroscopy images a feasible means of creating thickness maps for calcium and iodine in order to provide additional information regarding calcified lesions?*

1.2 Clinical and Technical background

1.2.1 Peripheral arterial disease

Peripheral Arterial Disease (PAD) is defined as the manifestation of atherosclerotic plaque in the arteries supplying the head, organs and limbs, limiting the flow of blood to the tissues supplied by these arteries. In practice, PAD usually refers to obstruction of blood flow to the lower extremities. PAD may give rise to symptoms such as claudicatio intermittens (CI) and rest pain, which may progress to critical limb ischaemia (CLI). The prevalence of symptomatic chronic obstructive PAD in the open population in the Netherlands, measured using the ankle-brachial index (<0.9), is estimated to be 7% in people at 55 years old, and 56% at 85 years and above. PAD is an expression of general vascular disease and they share the same risk factors such as smoking, diabetes mellitus and hypertension.[1] The Fontaine classification is used to classify the extent of PAD. Higher stages in this classification correspond with increasingly inhibiting symptoms (table 1.1). The primary diagnostic tool for PAD is the ankle-brachial index (ABI), which is defined as the peak systolic pressure in the ankle (A. dorsalis pedis or A. tibialis posterior, whichever is highest) divided by the peak systolic pressure in the arm (A. brachialis). A lower ABI corresponds with a higher degree of obstruction of bloodflow (table 1.2).

Table 1.1 Fontaine classification

Grade	**Symptoms**
I	Asymptomatic
II	Claudicatio Intermittens (CI)
IIa	Pain after walking >200m
IIb	Pain after walking <200m
III	Rest/nocturnal pain
IV	Necrosis and/or gangrene

Table 1.2 Ankle-brachial index

ABI	**Interpretation**
>1.3	False elevation; heavy vessel calcification
1.0-1.29	Normal
0.91-1.0	Borderline
0.7-0.9	Mild PAD
0.4-0.69	Moderate PAD
<0.4	Severe PAD, critical limb ischaemia

1.2.2 treatment options

Supervised exercise programs have been recommended as first-line therapies for the treatment of claudication symptoms in PAD.[2] Regular exercise may reduce pain symptoms and increase patient mobility. In acute care settings or exercise therapy fails, revascularization may be needed. Revascularization can be performed by either open or endovascular surgery, or a combination of both techniques. Open intervention involves the removal of the atherosclerotic buildup (endartherectomy) or circumventing the occluded artery using either a venous or synthetic graft (bypass). Endovascular procedures rely on making a small incision in the femoral artery, after which various catheters can be guided through the bloodstream to the target area using angiographic imaging. Usually a catheter containing a small balloon is guided to the occluded area and inflated in order to increase the diameter of the vascular lumen (PTA) and thereby restore blood flow. Drug coated balloons (DCB) and stent placement are also routinely used in combination with Percutaneous Transluminal Angioplasty (PTA) based on severity and location of the occlusion and composition of the atherosclerotic plaque (see fig. 1.3). Compared with open surgical revascularization of PAD, endovascular procedures offer lower peri-procedural risk rates, although initial success rates with occlusive disease are lower.[3] Nevertheless, nowadays endovascular revascularization is generally the first choice when surgical intervention is needed.

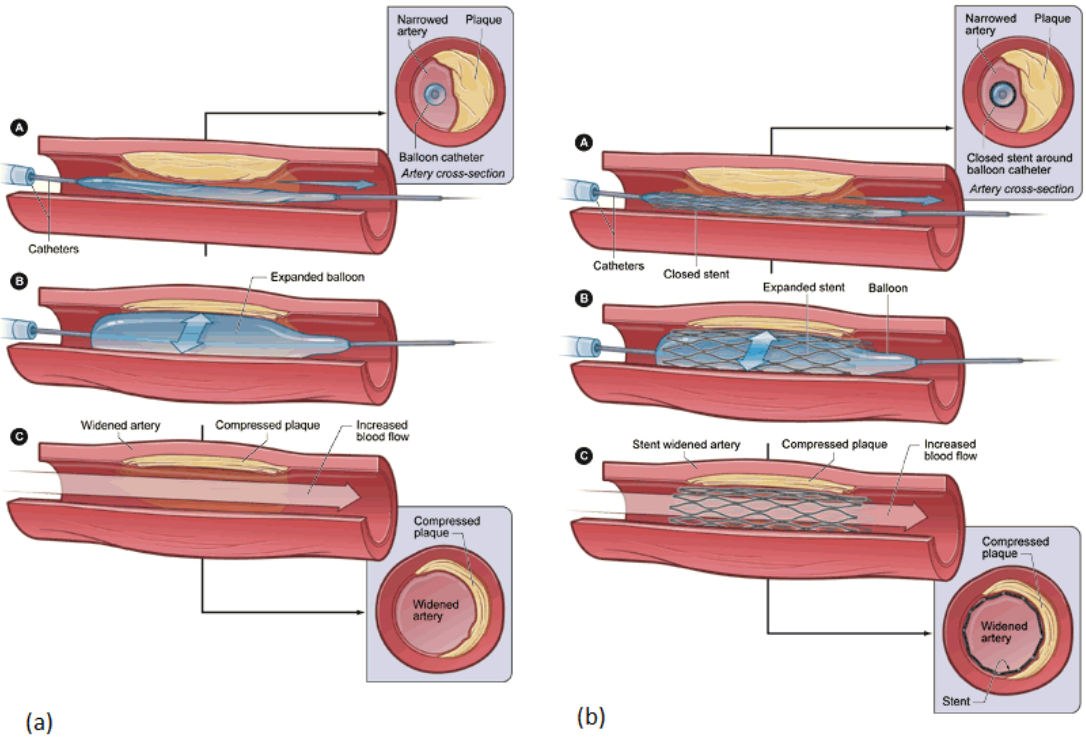

Fig. 1.1 (a) Percutaneous balloon angioplasty **(b)** Balloon-expandable stenting.

1.2.3 Fluoroscopic imaging and the Hybrid operating theater

In the hybrid operating theater of the UMC Utrecht, a ceiling mounted c-arm angiography system is used for imaging during endovascular interventions (fig. 1.2).

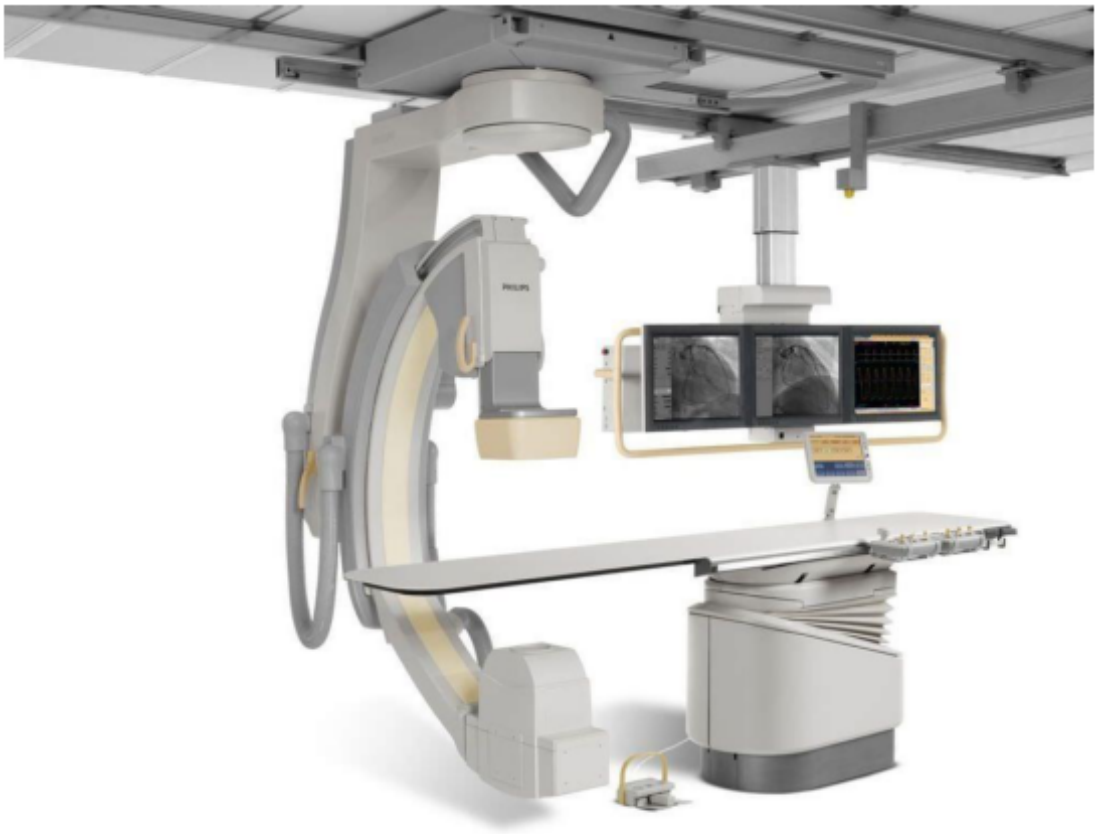

Fig. 1.2 The ceiling mounted Philips Allura Xper FD20 Flexmove fluoroscopy system.

Angiography and fluoroscopy are imaging techniques which employ the use of X-rays. An important distinction from regular x-ray imaging is that fluoroscopy allows for continuous imaging of the target area, allowing the operator to keep track of endovascular changes in real time. Angiography allows for imaging of the vascular lumen, which by itself is indistinguishable from surrounding tissues on x-ray images since blood and body tissues have similar X-ray attenuation coefficients. A digital subtraction angiography (DSA) image is therefore made, which highlights the changes in image intensity over time. An iodine-based contrast agent is injected into the bloodstream while capturing the DSA image, highlighting the lumen by changing its attenuation coefficient (see fig. 1.3). Exposing the patient to contrast medium is not without risk, however, since it may cause nephrotoxic side-effects, especially in patients who already exhibit reduced renal function.[4] The risk of exposure to ionizing radiation has also been widely documented and is well understood. Nevertheless, the risk of open surgery, or not performing surgery at all, generally outweighs the risk of exposing the patient to the harmful side-

effects of endovascular intervention. Minimizing these side-effects should, however, be an ongoing research goal.

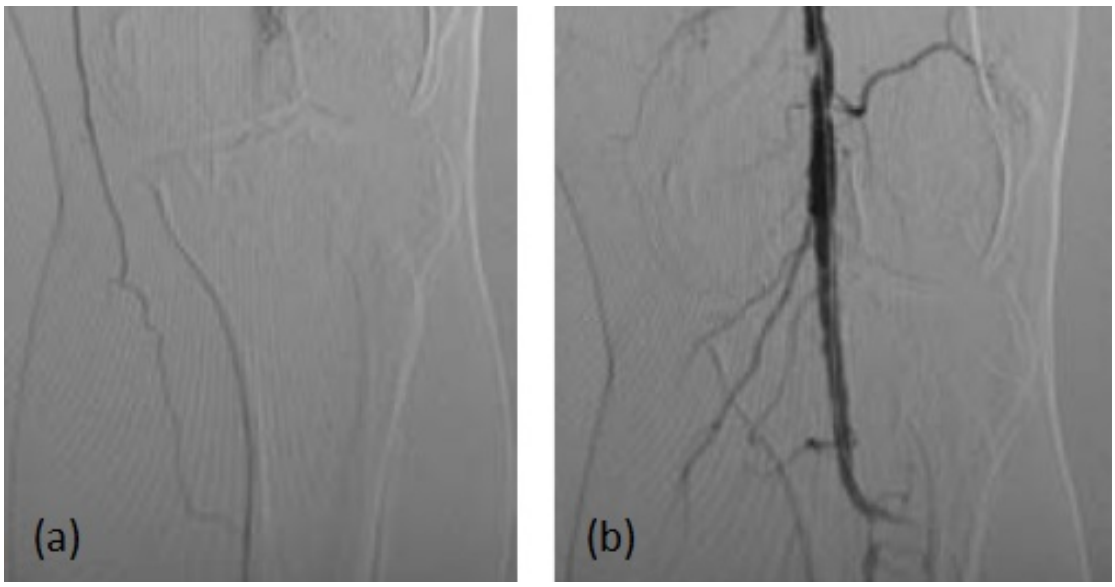

Fig. 1.3 (a) DSA image without contrast in the popliteal artery. The arterial lumen is not visible. **(b)** DSA image with intravenous contrast agent, allowing the popliteal artery to be distinguished from surrounding tissues.

1.2.4 Scattered radiation

In addition to exposing the patient to ionizing radiation, x-ray imaging subjects operating theater personnel to the same radiation through the process of scattering. When an x-ray beam enters the patient, a large portion of these photons produce scattered radiation through Compton interactions (fig. 1.4) While this scattered radiation is not uniform in all directions, there is no direction which is free from scatter. The amount of scattered radiation depends on the amount and composition of tissue in the primary x-ray beam as well the energy spectrum of the primary beam. While the patient receives a far greater radiation dose from the primary x-ray beam than the operating staff does from scattered radiation, patients do not routinely undergo these procedures. Operating room personnel may be subjected to scattered radiation daily, leading to chronic exposure and substantial annual doses. Any reduction in the occupational radiation dose for operating theater personnel is therefore desirable and in accordance with the As Low As Reasonably Achievable (ALARA)-principle. [5]

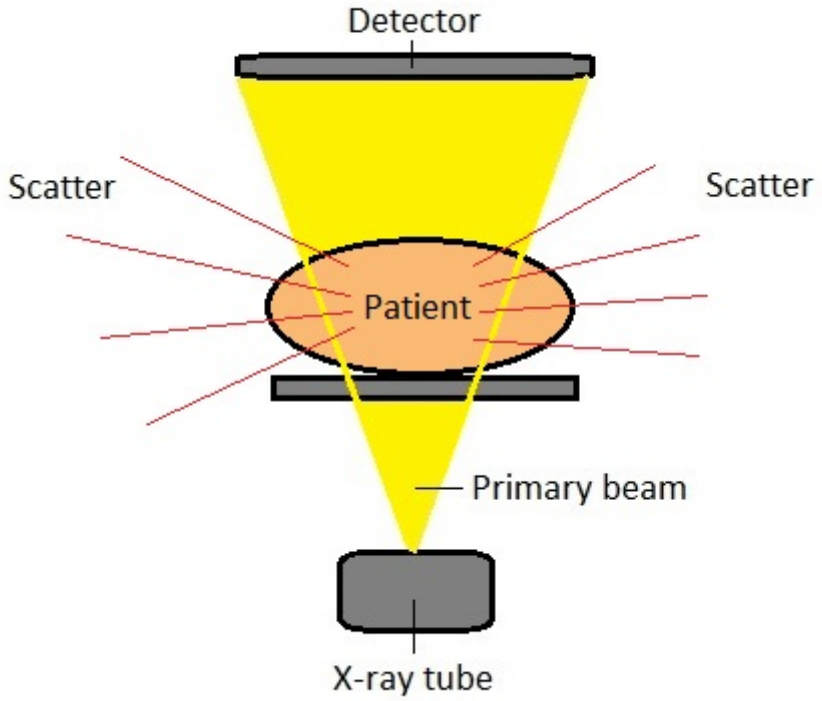

Fig. 1.4 Compton interactions between the primary x-ray beam of the imaging system and the patient produce scattered radiation. This radiation is the primary contributor to the occupational dose of hybrid operating theater personnel.

CHAPTER 2

Reduction of scatter-induced operator dose by means of a radiation absorbing sterile drape

2.1 Abstract

Background
This study assesses the feasibility of a radiation absorbing sterile drape in reducing the operator dose by scattered radiation during peripheral endovascular procedures.
Materials and methods
Fourty-nine patients who underwent endovascular peripheral stenting, balloon angioplasty or rotary atherectomy were included. Lead free radiation absorbing sterile drapes (Radpad®, Worldwide Innovations and Technologies Inc, KS, USA) were used during 25 procedures (study group), while 24 procedures were performed without the drapes (control group). Electronic personal dosimeters were placed at chest height of the first and second operators to measure unshielded body dose. DAP-adjusted dose was calculated in order to compensate for differences in baseline characteristics between the control and study groups. *Mann-Whitney U* testing was used for cumulative dose analysis. A multivariate mixed model analysis was used for *per-run* dose analysis.
Results
tatistical analysis resulted in a median dose reduction of 64% for cumulative dose analysis ($p<0.01$). A mean reduction of 80% was found in *per-run* dose analysis ($p<0.01$).
Conclusion
Usage of the drape resulted in statistically significant operator dose reduction rates while presenting no significant drawbacks during these procedures.

2.2 Introduction

Advances in endovascular treatment techniques have accelerated the use of fluoroscopy-guided procedures in the treatment of PAD over the last 20 years. [6–10] As these procedures become more common, so does the potential for exposure of Operating Room (OR) personnel to scattered radiation. Standard radiation protection protocols require the use of personal lead aprons and thyroid collars as well as the employment

of radiation absorbing floor-, table- or ceiling-mounted lead screens. While these measures may reduce personal absorbed doses significantly, stochastic effects of scattered radiation remain a cause of concern. Recent studies show that chronic low-level radiation exposure, even below the permissible limits based on the International Commission on Radiological Protection (IRCP), are linked to adverse biological effects.[11] Therefore, efforts should be made to further reduce occupational doses, in keeping with the As Low As Reasonably Achievable (ALARA)[5] principle. A number of recent studies have shown that the use of a disposable radiation absorbing drape significantly reduces operator dose during certain interventions by 23% to 80%. [12–17] This prospective study was undertaken in order to further assess the efficacy of the use of such a radiation absorbing drape during peripheral endovascular interventions.

2.3 Materials and methods

2.3.1 Patients

We conducted a single center prospective observational study. Patients undergoing endovascular intervention for peripheral arterial occlusive disease between February 2016 and November 2017 at the University Medical Center of Utrecht were included. Interventions involving the use of percutaneous transluminal angioplasty (PTA), drug-coated balloon (DCB), atherectomy or stent devices (or a combination thereof) were included. All interventions took place at the iliac, femoral, popliteal or crural arterial level (or a combination thereof). A power calculation based on the results of a prior study [18] revealed a sample size of 20 was required in order to reach a power of 0.9 with 95% confidence. All included procedures were performed in a hybrid OR equipped with a Philips Allura Xper FD20 Flexmove system with ClarityIQ technology (Philips Healthcare Systems, Best, the Netherlands).

2.3.2 Radiation shielding

The radiation absorbing sterile drape used is available commercially (RADPAD # 5511, Worldwide Innovations and Technologies Inc, KS, USA). This lead free shield (further referred to as "RADPAD") contains bismuth and has been certified by the manufacturer as a 0.375mm lead equivalent (personal communication, November 3, 2017). Cases included in the study group involved the use of either one or two RADPADs, based on the position of OR personnel and the C-arm relative to the operating table. When both operators were positioned on the same side of the table, one RADPAD was used. When the first and second operator were positioned on opposite sides of the table, a second RADPAD was added in order to provide protection for both operators. The position of OR personnel and C-arm differed between cases based on the type and anatomical

location of the intervention and operator preference (fig. 2.1). The RADPADs were placed on the patient's leg or hip in such a way that it was located between the operator and the irradiated area, allowing the operator is situated in the "shadow" of the RADPAD. Effort was taken to keep the RADPAD outside of the primary beam at all times, as placement within the primary beam can increase the skin entrance dose [12]. Usual attention was paid to good clinical practice such as adequate collimation, the use of low-radiation imaging protocols and minimizing detector height, in accordance with the ALARA principle. Further standard radiation shielding consisted of table-mounted lead drapes, ceiling mounted lead screens and a wheeled lead screen used by the anesthesiologist. The number of ceiling screens used (one or two) also depended on OR personnel and C-arm orientation. Personal shielding for all OR personnel consisted of a lead apron and thyroid collar.

2.3.3 Dosimetry

Electric personal dosimeters (PDM) of the DoseAware Xtend© system (Philips Healthcare, Best, the Netherlands) were used to record the dose of the first operator (FO) and second operator (SO). The PDMs were placed outside of the lead apron, at chest height to record the unshielded personal dose, at 10mm tissue depth (Hp(10)). In order to account for possible underestimation of FO or SO dose due to inadvertent shielding of the PDM by either the lead apron of the wearer or the lead apron of the other operator, the maximum operator dose was determined for each measurement and used in the statistical analysis. Measurement data of the DoseAware Xtend system was stored in a DICOM formatted DoseAware report. Reports of Fluoroscopy Time (FT), Air Kerma

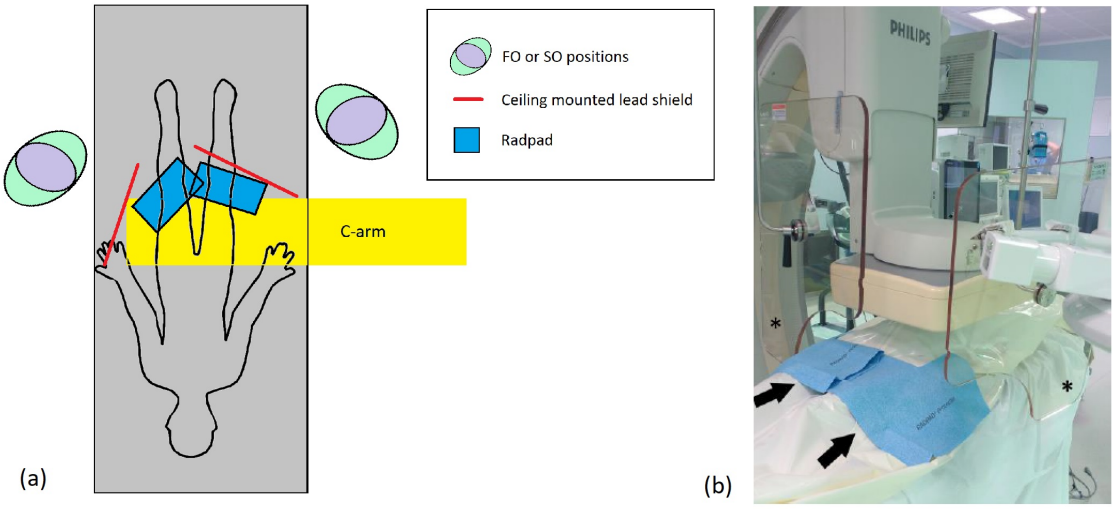

Fig. 2.1 (a) Example of possible FO and SO positions during endovascular intervention at the femoral level. **(b)** Example of ceiling screen (asterisks) and RADPAD (arrows) placement.

(AK), dose are product (DAP), kilovolt peak (kVp), milliampere-second (mAs), filtering, location and rotation of the C-arm, detector field size, number of frames and run duration were automatically generated by the C-arm system. Demographic information such as gender, age and BMI were obtained from the electronic patient record (EPR). Procedures were labeled according to the anatomical location of the treated artery: Iliac, femoral, popliteal/lower leg, and combinations thereof. Procedural and demographic information was combined with dose reports from the imaging system and PDM reports using MATLAB®.

2.3.4 Statistical analysis

In order to compensate for the effects of patient BMI and irradiation duration on the measured dose, Dose Area Product (DAP)-adjusted maximum operator dose was used as the primary outcome measure. Irradiation duration in and of itself was not compensated for since its effects are accounted for when compensating for DAP. DAP-adjusted maximum operator doses were calculated for each imaging run by dividing maximum operator dose by the cumulative DAP for the associated run. The natural logarithm of the DAP-adjusted maximum operator dose was used in order to account for heteroskedasticity and exponential distribution of the data. Since logarithmic transformation of zero readings would render statistical analysis impossible, these readings were replaced with 50% of the lower detection doserate limit of the Personal Dosimeter (PDM) (40 mSv/h) multiplied with the irradiation duration of the associated imaging runs.

Cumulative dose: Mann-Whitney U testing was used in order to compare both the uncompensated and DAP-adjusted cumulative maximum operator dose for the intervention and control groups.

Dose per run: We used R (R Core Team, 2016) and the *lme4* package (Bates, Maechler, Bolker and Walker, 2015) in order to perform a linear mixed effects analyses of the relationship between DAP-adjusted maximum operator dose per run and the use of the RADPAD: one model for all fluoroscopy runs and one for all DSA runs (a run was defined as one continuous press of the C-arm foot pedal). In order to resolve non-independence caused by having repeated measurements from the same patient, data was clustered by patient. Intervention location, C-arm angulation, number of ceiling screens used and the presence of RADPADs were assessed in these models as fixed effects. Residual plots were visually inspected for signs of any deviations from homoscedasticity or normality. P-values were obtained by likelihood ratio tests of the full model with the effect in question against the reduced model without the effect in question. The results of the mixed effects models were further elaborated by calculating

odds ratios.

2.4 Results

Table 2.1 Patient characteristics and procedure details

Patient/procedure details	**Control group** (n=24)	**Study group** (n=25)	**p-value**
Mean age	70.1	64.8	0.04*
Mean BMI	27.90	25.47	0.06
Gender = male (%)	15 (62.5)	12 (48)	0.46
Median fluoroscopy time (IQR)	1071 s (814-1626)	781 s (367-1324)	0.07
Median DAP (IQR)	30.1 $Gycm^2$ (17.9-77.5)	26.4 $Gycm^2$ (8.0-47.5)	0.26
Procedures with one ceiling screen (%)	14 (58.3)	10 (40)	

*Statistically significant

Table 2.2 Procedure locations and RADPADs used

Procedure location	**Control group** (n=24)	**Study group** (n=25)	**One RADPAD** (n=17)	**Two RADPADs** (n=8)
Iliac	9	12	8	4
Femoral	12	12	8	4
Lower leg	3	1	1	0

Fourty-nine patients were included in the analysis; 25 patients in the study group and 24 patients in the control group. Patient and procedure characteristics, as well as a breakdown of procedure locations and RADPAD usage are listed in tables 2.1 and 2.2. The control and study group were comparable in terms of radiation-associated characteristics, including BMI, fluoroscopy time, DAP and the use of ceiling screens.

Dose per run: A total of 8264 fluoroscopy runs and 756 DSA runs were acquired during the 49 included procedures. After removing runs where no DAP reading was available (rendering the calculation of DAP-adjusted maximum operator dose impossible), 8176 fluoscopy runs (3581 study, 4595 control) and 756 DSA runs (327 study, 429 control) remained. Likelihood ratio testing showed the presence of the RADPAD to be significant for all datasets (fluoroscopy runs, DSA runs, and total runs). Intervention location and the number of ceiling screens were found not to be significant in all subsets and were therefore not used in the mixed effects analysis. C-arm angulation was found not to be significant in the DSA subset but significant in the fluoroscopy and total datasets, and was therefore not used in the DSA subset (table 2.3). Subsequent analysis showed that the presence of RADPADs was significantly associated with a reduction in DAP-adjusted dose in the fluoroscopy (odds ratio, 0.201; $P<0.01$), DSA (odds ratio, 0.142; $P<0.01$) and total (odds ratio, 0.197; $P<0.01$) datasets. C-arm angulation was found

Table 2.3 Likelihood ratio tests

Factor	chi-squared	p-value
Fluoroscopy:		
Location	1.965	0.37
Ceiling screens	0.053	0.82
C-arm angulation	4.261	0.04*
RADPAD	12.69	<0.01*
DSA:		
Location	4.286	0.12
Ceiling screens	0.507	0.48
C-arm angulation	1.950	0.16
RADPAD	9.313	<0.01*
Total:		
Location	2.197	0.33
Ceiling screens	0.029	0.87
C-arm angulation	3.846	0.05*
RADPAD	12.78	<0.01*

*Statistically significant

to be significant in the fluoroscopy dataset only (Odds ratio, 1.006; p = 0.04). (table 2.4)

Cumulative dose: A significant reduction in cumulative DAP-adjusted maximum operator dose of 62% was found between the control and study groups for DSA runs (p<0.01), 74% for fluoroscopy runs (p<0.01) and 64% for the total dataset (p<0.01). A significant reduction in the uncompensated operator dose of 75% was found for DSA runs (p<0.01), 90% for fluoroscopy runs (p<0.01) and 81% for the total dataset (p<0.01). (figs 2.2, 2.3)

Table 2.4 Multivariate analysis of *Dose per run* data

Dataset	DAP-adjusted dose (mSv/Gycm^2)	OR (95% CI)	p-value
Fluoroscopy:			
Intercept	2.451×10^{-4}		
Angle	2.466×10^{-4}	1.006 (1.000 - 1.012)	0.04*
RADPAD	4.918×10^{-5}	0.201 (0.088 - 0.459)	<0.01*
DSA:			
Intercept	8.083×10^{-4}		
RADPAD	1.145×10^{-4}	0.142 (0.042 - 0.471)	<0.01*
Total:			
Intercept	2.758×10^{-4}		
Angle	2.773×10^{-4}	1.006 (1.000 - 1.012)	0.05*
RADPAD	5.435×10^{-5}	0.197 (0.085 - 0.455)	<0.01*

*Statistically significant

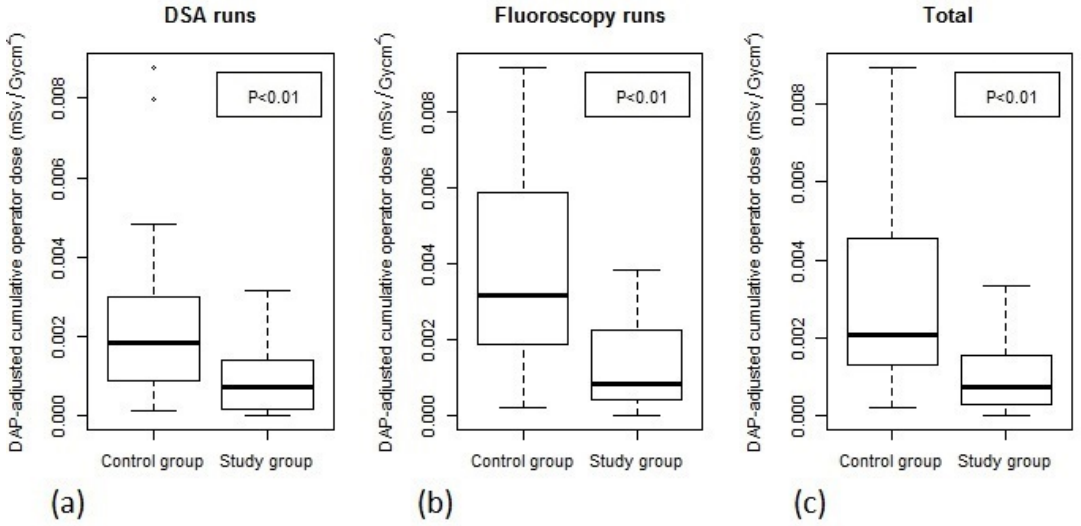

Fig. 2.2 Cumulative DAP-adjusted operator doses for the control group (n=24) and study group (n=25): **(a)** DSA runs, **(b)** fluoroscopy runs, **(c)** total dataset.

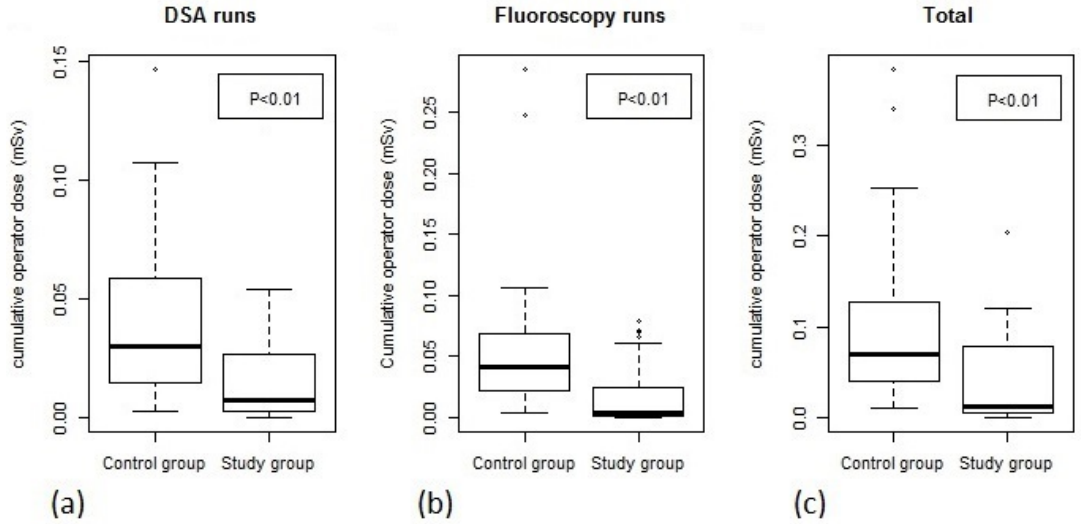

Fig. 2.3 Cumulative uncompensated operator doses for the control group (n=24) and study group (n=25): **(a)** DSA runs, **(b)** fluoroscopy runs, **(c)** total dataset.

In practical terms: In our control group an unshielded median operator dose of 0.071 mSv per procedure was found. When applying our found reduction rates for the total dataset of 64% and assuming 100 peripheral endovascular interventions per operator per year, a radiation dose reduction of 4.5 mSv per year is found. This amounts to 23% of the yearly permissible dose for radiation workers.[19]

2.5 Discussion

This prospective study shows that the use of a radiation absorbing sterile drape during fluoroscopy-guided peripheral arterials interventions is feasible and significantly reduces the occupational radiation exposure for the operator. Previous studies with radiation absorbing sterile drapes during pectoral device implantation [14], electropysiology procedures [13], cardiac resynchronization therapy [16], complex percutaneous coronary intervention procedures [17] and EVAR procedures [18] all show a similar significant reduction in operator radiation exposure. Of particular note is a previous study of the RADPAD during peripheral arterial interventions. [15] While this study is limited to per-procedure cumulative data analysis, it does show a similar reduction of operator dose when compared to both our cumulative and *per-run* data analyses.

In addition to being inexpensive, the RADPAD proved to be easy to position and was not associated with any complications or safety issues during the intervention. The RADPAD did enter the primary beam during several procedures, but further collimation was generally sufficient in remedying this problem. In other cases, repositioning of the RADPAD was necessary but proved to be quick and easy.

In addition to reducing the occupational radiation dose at chest level, the RADPAD may be able to simultaneously reduce the dose at eye level as well. Recent studies show that the risk of cataract due to radiation may have been underestimated in the past, with threshold doses found below the previously set threshold of 2 Gy and suggesting there may not be a threshold dose at all.[20–22] In response to this new information, in 2012 the ICRP have adjusted the permissible occupational eye dose from 150 mSv/year to 20 mSv/year (averaged over a period of 5 years, with no single year exceeding 50 mSv).[19] In light of these changes, extra care should be taken to further reduce the occupational dose to the eye. The RADPAD may prove to be a valuable asset in the pursuit hereof by being able to shield the entire upper body from harmful radiation. One pilot study reported a reduction in eye dose when using the RADPAD in peripheral endovascular procedures, although statistical significance was not reached.[15] Further study is necessary in order to assess the efficacy of the RADPAD for this purpose.

Limitations

A wide array of variables such as fluoroscopy time, Kilovolt Peak (kVp) and Milliampresecond (mAs), fluoscopy/DSA ratio may have a significant effect on patient exposure (DAP) during procedures, and therefore contribute to differences in measured OR personnel dose. By using DAP-adjusted dose as the primary outcome parameter, standardization of all these variables is made possible. A potential drawback of this method is that it assumes a linear relationship between the measured maximum operator dose and the DAP of the associated imaging run. Conclusive evidence for such linear behaviour

was not found (see Appendix fig. A.4). However, evidence for a different relationship (e.g. exponential) was not found either.
About half of all *per-run* maximum operator dose readings reported zero dose. While it is logical to assume that the presence of the RADPAD may give rise to an increase in measured zero values, this is not the only reason for such measurements to occur. Zero readings may also arise from the operators inadvertently shielding their PDM with their lead apron (by turning away from the radiation source) or being shielded by either the other operator or the sterile nurse. It would be unfeasible to assess the validity of each zero reading and exclusion of these "false-positives" is therefore impossible. Exclusion of all zero readings would solve this problem, but would lead to an exclusion of "true-positive" zero readings, which is valuable data and may alter the outcome of the study. Therefore, the choice was made to include all zero readings under the assumption that the chance of occurrence of false negative readings is random, and should therefore be roughly equal among both the study and control groups.
With the data being skewed to the lower end of the doserate spectrum, most recorded runs were presumably either just below or just above the lower PDM threshold. A substantial amount of our data consists of zero readings due to the fact that the readings below the threshold were not registered and therefore set to zero. In case of the *per-run* analysis the zero readings were changed to 50% of the detection limit. Without knowledge regarding the distribution of the data below the threshold, we cannot exclude the possibility that most of these readings may have been relatively close to the detection limit. Changing all these values to either zero of 50% of the lower limit may therefore have lead to an overestimation of the dose reduction due to the RADPAD. However, our study does show similar dose reduction rated compared to a previous study. [15]

2.6 Conclusion

Results from this study suggest that the use of a disposable radiation absorbing sterile drape significantly reduce the operator dose from scattered radiation during peripheral endovascular interventions. Use of the drape during these procedures resulted in a median reduction of 64% found in cumulative dose analysis and a mean reduction of 80% found in *per-run* multivariate analysis. Usage of the drape presented no significant drawbacks for the operator.

CHAPTER 3

Assessing the feasibility of dual-energy fluoroscopy images in creating calcium and iodine thickness maps

3.1 Abstract

Background
This study assesses the use of fluoroscopic images at discrete energy levels in creating calcium and iodine maps. These maps are aimed at providing the vascular surgeon with additional means to cross difficult to navigate arterial occlusions, thereby reducing imaging time and radiation exposure for both the patient and operating theater personnel.
Materials and methods
Custom imaging protocols were created in order to create images at the maximum achievable effective energy separation. A BMD algorithm was created in order to create density maps for iodine and calcium. A cadaver experiment was performed in order to simulate an intervention of a calcified lesion in a peripheral artery.
Results
Two sets of calcium and iodine maps were created, based on different calculations of effective photon energy.
Conclusion
These maps did not seem to provide additional information regarding the extent and morphology of the calcified lesions present in the images when compared to the regular fluoroscopy images. Negative values for iodine thickness indicate that further research is needed in order to calibrate the BMD protocol. A phantom study is recommended in order to further assess the feasibility of dual-energy techniques in fluoroscopic imaging.

3.2 Introduction

An alternate way of reducing the occupational radiation exposure of operating theater personnel is to reduce the number of radiation runs as well as the duration of each run. During interventions targeting PAD, it is imperative for the surgeon to navigate through the occlusive lesion with a guidewire prior to performing PTA or stenting. However,

occlusive lesions may be difficult to cross, thereby increasing imaging time and radiation exposure. The difficulty of navigating the lesion may be attributed to an inadequate contrast between arterial lumen and the (calcified) lesion. Without sufficient knowledge about the extent, composition and morphology of the lesion, it may be difficult for the surgeon to make a well-informed decision as to how to navigate through it.
It has been known since the 70s that additional information regarding the different substances and tissues in CT imaging may be acquired by imaging at multiple energy levels. Although the potential of this technique was apparent, its use was limited due to technical limitations.[23] Recent advances in CT technology have sparked new interest in dual-energy applications, and dedicated dual-energy CT scanners continue to be developed.
Our aim is to increase the information of the local vascular environment available to the surgeon by translating the technique of dual-energy imaging to the hybrid operating theater. We propose the use of a Basic Material Decomposition (BMD) algorithm based on dual energy fluoroscopy images in order to create calcium and iodine thickness maps. These maps may provide increased contrast between the contrast agent in the arterial lumen and the calcified lesions in the arterial wall. This, in turn, may allow for faster navigation of the lesion, leading to a decrease in imaging time and radiation dose for both patient and operating theater personnel.

3.3 Materials and methods

3.3.1 Imaging system and protocols

In order to perform BMD on fluoroscopy images, two image datasets at two discrete energy levels are needed. While Dual-Energy CT systems may obtain these two datasets in a single imaging run, there are currently no fluoroscopy systems with this capability. We therefore collaborated with Philips in the creation of several custom imaging protocols for the fluoroscopy system in the experimental Hybrid operating theater setup at our disposal, the Philips Allura Xper FD20 Flexmove system (Philips Healthcare Systems, Best, the Netherlands). These protocols were stripped of most of the standard software-based image post-processing in order to images with minimal undesirable alterations. Furthermore, in order to obtain the maximum reasonably achievable energy separation between the two datasets, the high energy protocol was set at 120 KvP; the upper limit of the x-ray tube. The low energy protocol was set at 80 KvP; the lowest energy possible without sacrificing significantly on Signal-to-Noise Ratio (SNR). In addition to the standard 1mm primary beam filter, a 0.1mm copper filter and a 0.4mm copper filter were chosen for the 80KvP and 120KvP protocols, respectively, in order to further increase the effective energy separation.

3.3.2 Cadaver experiment

The created protocols were installed on fluoroscopy system of the experimental Hybrid operating theater setup of the Gemeenschappelijk Dierenlaboratorium (GDL), which is where we performed subsequent imaging. In order to simulate an intervention of a calcified lesion in a peripheral artery as closely as possible, a fresh-frozen human cadaveric leg was used for imaging. Previous imaging of the same leg showed that extensive calcification was present in the iliac and femoral arteries. Prior to imaging, the leg was flushed with a mild soap solution in order to evacuate any residual coagulated blood, after which a 20% solution of contrast agent in water was injected into the iliac artery, displacing the soap solution and filling the arteries. The artery was then clamped shut in order to retain the contrast agent solution inside the vasculature.
Imaging was then performed using the customized fluoroscopy protocols. Image datasets at 80 KvP and 120 KvP were created at the femoral, popliteal and crural level.

3.3.3 Basic material decomposition

In order to provide the surgeon with additional information about the extent, composition and morphology of the target lesion, some sort of image which contains information about the amount of contrast agent (iodine) and calcification (Calcium) in each imaged pixel is needed.
According to research done by Alvarez and Macovski, the image intensity I can be defined as a function of the x-ray source intensity I_0, the thickness of the different tissues d along x-ray beam path L and their relative attenuation coefficients μ. [23] This relationship between input intensity, tissue parameters and output (image) can be described as:

$$I = I_0 * e^{(-\mu_I * d_I - \mu_c * d_c)} dL \tag{3.1}$$

In our case, we obtain two equations for our two discrete energy levels of 120 and 80 KvP:

$$I_{120} = I_{0,120} * e^{(-\mu_{I,120} * d_I - \mu_{c,120} * d_c)} dL \tag{3.2}$$

$$I_{80} = I_{0,80} * e^{(-\mu_{I,80} * d_I - \mu_{c,80} * d_c)} dL \tag{3.3}$$

Which may be rewritten such that:

$$\mu_{I,120} * d_I + \mu_{c,120} * d_c = ln(I_{0,120}) - ln(I_{120}) = ln(\frac{I_{0,120}}{I_{120}}) \tag{3.4}$$

$$\mu_{I,80} * d_I + \mu_{c,80} * d_c = ln(I_{0,80}) - ln(I_{80}) = ln(\frac{I_{0,80}}{I_{80}}) \tag{3.5}$$

Equations 3.4 and 3.5 can be represented in matrix form:

$$\begin{bmatrix} \mu_{I,120} & \mu_{c,120} \\ \mu_{I,80} & \mu_{c,80} \end{bmatrix} \begin{bmatrix} d_I \\ d_c \end{bmatrix} = \begin{bmatrix} ln(\frac{I_{0,120}}{I_{120}}) \\ ln(\frac{I_{0,80}}{I_{80}}) \end{bmatrix} \tag{3.6}$$

The attenuation coefficients of iodine and calcium at 80 and 120 KvP are dependent on the effective photon energies E_{eff} of the x-ray beam at these anode voltages. Since E_{eff} could not be obtained experimentally, these values were obtained from literature by researching E_{eff} values as a function of anode voltage and filter composition.[24] By comparing the attenuation coefficients of aluminium and copper at 80 and 120 KeV using the x-ray mass attenuation coefficient tables provided by the National Institute of Standards and Technology (NIST), aluminium equivalents for the filters used during the respective imaging procedures were obtained.

For the 120 KeV image shot through a filter containing 1mm aluminium and 0.1mm copper:

$$1mmAl + 0,1mmCu = 1mmAl + (\frac{0.1}{\alpha})mmAl \tag{3.7}$$

Where:

$$\alpha = \frac{\mu_{Al,120}}{\mu_{Cu,120}} \tag{3.8}$$

And for the 80 KeV image shot through a filter containing 1mm aluminium and 0.4mm copper:

$$1mmAl + 0,4mmCu = 1mmAl + (\frac{0.4}{\beta})mmAl \tag{3.9}$$

Where:

$$\beta = \frac{\mu_{Al,80}}{\mu_{Cu,80}} \tag{3.10}$$

The attenuation coefficients of Iodine and Calcium at these effective energies were obtained using the same tables provided by the NIST.[25] Both the image intensity and x-ray source intensity levels were obtained during our experiment. By obtaining the values for the attenuation coefficients of iodine and calcium at the appropriate effective energies as well as the image and source intensities two equations with two unknowns were obtained, which were solved for D_I and D_c using MATLAB®.. By repeating this

process for each pixel in the images and combining the values for D_I and D_c in new matrices, the associated "thickness maps" for iodine and calcium were created.
A second set of thickness maps were created by approximating E_eff as roughly 60-70% of the anode voltage. The effective photon energy levels for these images were set at 50 and 80 KeV for the 80 and 120 KV anode voltage images, respectively.

3.4 Results

First dataset: Equivalent aluminium filter thicknesses of 2.25mm and 3.9mm were found for our 80KvP and 120 KvP images, respectively. The associated respective E_{eff} values obtained from literature were 34 KeV and 46 KeV. The calculated iodine and calcium thickness maps are presented along with the 80 and 120 KvP images on which they are based (fig. 3.1). Brighter pixels on the thickness maps correspond with a greater thickness of their respective elements. The calcium thickness map consists solely of positive values while the iodine map consists of negative values in this dataset.

Second dataset: This image contains thickness maps based on the same images as the first dataset but with different effective photon energy levels (fig. 3.2). These images contained similar positive pixel values for the calcium map and negative values for the iodine map.

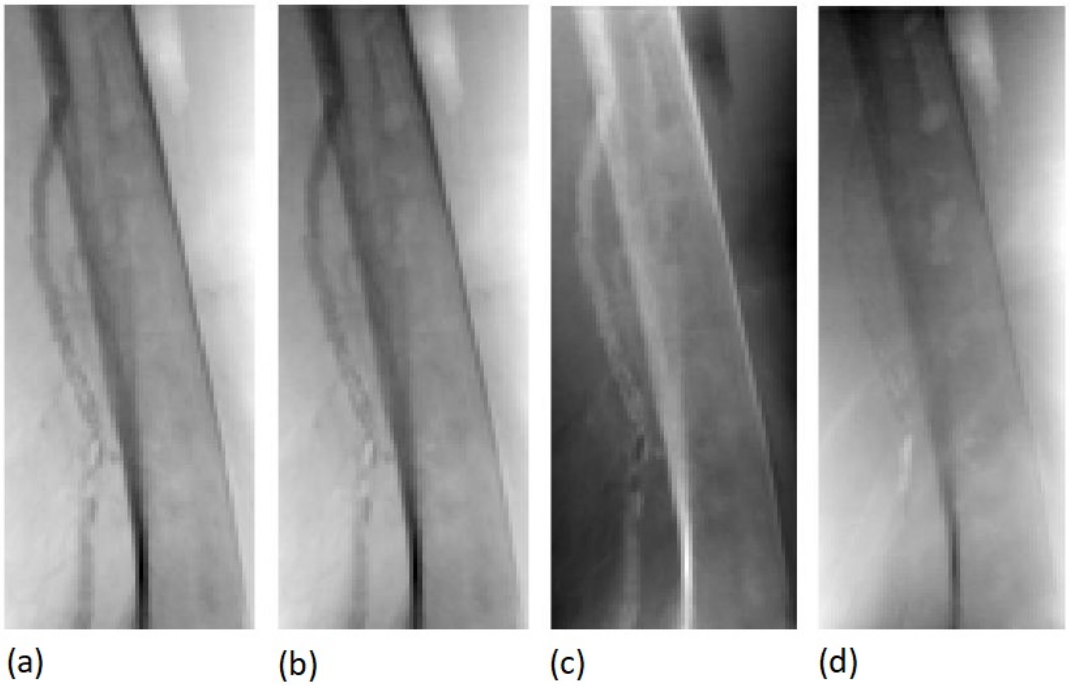

Fig. 3.1 Frontal views of the femoral section of a cadaveric leg. Included in the images is part of the femur as well as a calcified femoral artery, filled with contrast agent. **(a)** 80 KvP image **(b)** 120 KvP image **(c)** Calcium thickness map **(d)** Iodine thickness map

Fig. 3.2 Thickness maps created using E_eff values of 80 and 50 KeV for the 120 and 80 kV anode voltage pictures, respectively. **(a)** Calcium thickness map **(b)** Iodine thickness map

3.5 Discussion

The benefits of obtaining addition information on body tissue composition by acquiring images at different x-ray energy levels are becoming more and more apparent with the implementation of dual energy CT applications. In an effort to assess the feasibility of applying one of these techniques in a hybrid operating theater setup, we applied a BMD algorithm to dual energy images obtained using a fluoroscopy system.

Both the created dual energy images as well as the thickness maps for iodine and calcium show a clear delineation of the femoral cortex. The femoral edges are bright on the calcium thickness map and dark on the iodine map, which is in line with our expectations. However, a clear separation of the iodine-based contrast agent in the vascular lumen and the calcifications in the vessel wall is not present in these thickness maps. The entire artery is relatively homogeneously enhanced in both calcium maps while it is hard to distinguish from the surrounding tissue in the iodine map of the first dataset. The second iodine map resembles a direct negative image of the second calcium map. These supplementary images do not seem to present any additional information regarding the severity and morphology of arterial obstructions by calcification when compared to the base 80 and 120 KvP images.

While the iodine maps relatively closely resemble the original images, the calcium maps appear to be the inverse (negative) of the original images. When examining the pixel

values of the iodine maps we found only negative values, something which clearly does not accurately represent the presence of iodine in these pixels.
A possible cause for this error may be found in the choice of effective photon energy values which were obtained by expressing the attenuation of the aluminium and copper filters in our fluoroscopy system as a pure aluminium filter. This may have lead to inaccuracies in determining the effective photon energies and the subsequent choice of mass attenuation coefficients for calcium and iodine. Furthermore, the effective energy of the 80 KvP image was calculated to be 34 KeV, which is very close to the K-edge of iodine at 33.2 KeV. Therefore even a small inaccuracy in the effective energy may lead to a vast over- or underestimation of the mass attenuation coefficient for this element. However, using higher effective energy levels for the second dataset did not seem to resolve this problem.
Another possible cause for poor separation of our two target materials (iodine and calcium) may be poor spectral separation of the high- and low-energy images. Modern dual-energy CT systems typically use anode voltages of 80 and 140 KvP for their low- and high-energy images, respectively, in order to achieve maximum spectral separation. Typical associated effective energy levels are 56- and 76 KeV, respectively, in second-generation dual-energy CT systems with typical filters.[26] Since anode voltages greater than 120 KV are not achievable in our fluoroscopy system, in addition to the fact that different filters are used, we are not able to achieve the same spectral separation as dual-energy CT systems.
A fresh-frozen human cadaveric leg was used in order to simulate an intervention of a calcified lesion in a peripheral artery. While this approach allows us to qualitatively assess the added benefits of the generated calcium and iodine maps, it is difficult to quantitatively assess them since the exact amounts of iodine and calcium present in the image are unknown. In order to effectively assess the effect of different parameters such as effective photon energy and mass attenuation coefficients on the generated calcium and iodine maps a phantom study may prove to be more feasible. By creating new 80 and 120 KeV images of an imaging phantom containing precisely documented amounts and distributions of iodine and calcium, the optimal input parameters for the BMD algorithm may be found iteratively in order to calibrate the protocol and assess whether the use of dual-energy techniques is feasible on a fluoroscopy system.

3.6 Conclusion

Calcium and iodine thickness maps based on dual-energy fluoroscopy images of the femoral region of a fresh-frozen human cadaveric leg were used in order to assess the feasibility of dual-energy techniques in a hybrid operating theater setting. The gener-

ated maps did not present any additional information regarding the severity and morphology of the arterial obstructions in the femoral artery when compared to regular fluoroscopy images. The presence of negative thickness values in the iodine maps indicates that further optimization of input parameters for the BMD protocol is needed. Further research involving a phantom study is recommended in order to assess the feasibility of dual-energy techniques in fluoroscopic imaging.

REFERENCES

[1] Marie-louise Bartelink, Bernard Elsman, Andrew Oostindjer, Jelle Stoffers, Tjerk Wiersma, and Jacques Geraets. NHG-Standaard 'Perifeer arterieel vaatlijden'. *Geneesmiddelenbulletin*, 48(6):68–69, 2014.

[2] M. Tendera, V. Aboyans, M.-L. Bartelink, I. Baumgartner, D. Clement, J.-P. Collet, A. Cremonesi, M. De Carlo, R. Erbel, F. G. R. Fowkes, M. Heras, S. Kownator, E. Minar, J. Ostergren, D. Poldermans, V. Riambau, M. Roffi, J. Rother, H. Sievert, M. van Sambeek, T. Zeller, J. Bax, A. Auricchio, H. Baumgartner, C. Ceconi, V. Dean, C. Deaton, R. Fagard, C. Funck-Brentano, D. Hasdai, A. Hoes, J. Knuuti, P. Kolh, T. McDonagh, C. Moulin, D. Poldermans, B. Popescu, Z. Reiner, U. Sechtem, P. A. Sirnes, A. Torbicki, A. Vahanian, S. Windecker, P. Kolh, A. Torbicki, S. Agewall, A. Blinc, M. Bulvas, F. Cosentino, T. De Backer, A. Gottsater, D. Gulba, T. J. Guzik, B. Jonsson, G. Kesmarky, A. Kitsiou, W. Kuczmik, M. L. Larsen, J. Madaric, J.-L. Mas, J. J. V. McMurray, A. Micari, M. Mosseri, C. Muller, R. Naylor, B. Norrving, O. Oto, T. Pasierski, P.-F. Plouin, F. Ribichini, J.-B. Ricco, L. Ruilope, J.-P. Schmid, U. Schwehr, B. G. M. Sol, M. Sprynger, C. Tiefenbacher, C. Tsioufis, and H. Van Damme. ESC Guidelines on the diagnosis and treatment of peripheral artery diseases: Document covering atherosclerotic disease of extracranial carotid and vertebral, mesenteric, renal, upper and lower extremity arteries * The Task Force on the Diagnosis and Treatment of Peripheral Artery Diseases of the European Society of Cardiology (ESC). *European Heart Journal*, 32(22):2851–2906, 2011.

[3] Arun K. Thukkani and Scott Kinlay. Endovascular Intervention for Peripheral Artery Disease. *Circulation Research*, 116(9):1599–1613, 2015.

[4] Anna M. Sailer, Michiel W. de Haan, Rick de Graaf, Willem H. van Zwam, Geert Willem H Schurink, Patricia J. Nelemans, Joachim E. Wildberger, and Marco Das. Fusion Guidance in Endovascular Peripheral Artery Interventions: A Feasibility Study. *CardioVascular and Interventional Radiology*, 38(2):314–321, 2015.

[5] World Health Organization. Basics of Radiation Protection; How to achieve ALARA, 2004.

[6] Vincent L Rowe, William Lee, Fred A Weaver, and David Etzioni. Patterns of treatment for peripheral arterial disease in the United States: 1996-2005. *Journal of vascular surgery*, 49(4):910–7, apr 2009.

[7] Philip P Goodney, Adam W Beck, Jan Nagle, H Gilbert Welch, and Robert M Zwolak. National trends in lower extremity bypass surgery, endovascular interventions, and major amputations. *Journal of vascular surgery*, 50(1):54–60, jul 2009.

[8] Teviah Sachs, Frank Pomposelli, Allen Hamdan, Mark Wyers, and Marc Schermerhorn. Trends in the national outcomes and costs for claudication and limb threatening ischemia: angioplasty vs bypass graft. *Journal of vascular surgery*, 54(4):1021–1031.e1, oct 2011.

[9] Roman Nowygrod, Natalia Egorova, Giampaolo Greco, Patrice Anderson, Annetine Gelijns, Alan Moskowitz, James McKinsey, Nicholas Morrissey, and K Craig Kent. Trends, complications, and mortality in peripheral vascular surgery. *Journal of vascular surgery*, 43(2):205–16, feb 2006.

[10] L Norgren, W R Hiatt, J a Dormandy, M R Nehler, K a Harris, F G R Fowkes, R B Rutherford, and TASC II Working Group. Inter-society consensus for the management of peripheral arterial disease. *Int Angiol*, 26(2):81–157, 2007.

[11] S Heydarheydari, A Haghparast, and M T Eivazi. A Novel Biological Dosimetry Method for Monitoring Occupational Radiation Exposure in Diagnostic and Therapeutic Wards: From Radiation Dosimetry to Biological Effects. *Journal of biomedical physics and engineering*, 6(1):21–6, mar 2016.

[12] J. N. King, A. M. Champlin, C. A. Kelsey, and D. A. Tripp. Using a sterile disposable protective surgical drape for reduction of radiation exposure to interventionalists. *American Journal of Roentgenology*, 178(1):153–157, 2002.

[13] Joseph J Germano, Gina Day, David Gregorious, Venkataraman Natarajan, and Todd Cohen. A novel radiation protection drape reduces radiation exposure during fluoroscopy guided electrophysiology procedures. *The Journal of invasive cardiology*, 17(9):469–72, sep 2005.

[14] Grant R Simons and William W Orrison. Use of a sterile, disposable, radiation-absorbing shield reduces occupational exposure to scatter radiation during pectoral device implantation. *Pacing and clinical electrophysiology : PACE*, 27(6 Pt 1):726–9, jun 2004.

[15] S. Power, M. Mirza, a. Thakorlal, B. Ganai, L. D. Gavagan, M. F. Given, and M. J. Lee. Efficacy of a Radiation Absorbing Shield in Reducing Dose to the Interventionalist During Peripheral Endovascular Procedures: A Single Centre Pilot Study. *CardioVascular and Interventional Radiology*, 38(3):573–578, 2015.

[16] Marco Brambilla, Eraldo Occhetta, Martina Ronconi, Laura Plebani, Alessandro Carriero, and Paolo Marino. Reducing operator radiation exposure during cardiac resynchronization therapy. *Europace : European pacing, arrhythmias, and cardiac electrophysiology : journal of the working groups on cardiac pacing, arrhythmias, and cardiac cellular electrophysiology of the European Society of Cardiology*, 12(12):1769–73, dec 2010.

[17] John C Murphy, Karen Darragh, Simon J Walsh, and Colm G Hanratty. Efficacy of the RADPAD protective drape during real world complex percutaneous coronary intervention procedures. *The American journal of cardiology*, 108(10):1408–10, nov 2011.

[18] C Kloeze, E G Klompenhouwer, P J M Brands, M R H M van Sambeek, P W M Cuypers, and J A W Teijink. Editor's choice–Use of disposable radiation-absorbing surgical drapes results in significant dose reduction during EVAR procedures. *European journal of vascular and endovascular surgery : the official journal of the European Society for Vascular Surgery*, 47(3):268–72, mar 2014.

[19] Authors on behalf of ICRP, F A Stewart, A V Akleyev, M Hauer-Jensen, J H Hendry, N J Kleiman, T J Macvittie, B M Aleman, A B Edgar, K Mabuchi, C R Muirhead, R E Shore, and W H Wallace. ICRP publication 118: ICRP statement on tissue reactions and early and late effects of radiation in normal tissues and organs–threshold doses for tissue reactions in a radiation protection context. *Annals of the ICRP*, 41(1-2):1–322, feb 2012.

[20] Eiji Nakashima, Kazuo Neriishi, and Atsushi Minamoto. A reanalysis of atomic-bomb cataract data, 2000-2002: a threshold analysis. *Health physics*, 90(2):154–60, feb 2006.

[21] Kazuo Neriishi, Eiji Nakashima, Atsushi Minamoto, Saeko Fujiwara, Masazumi Akahoshi, Hiromu K Mishima, Takashi Kitaoka, and Roy E Shore. Postoperative cataract cases among atomic bomb survivors: radiation dose response and threshold. *Radiation research*, 168(4):404–8, oct 2007.

[22] A K Junk, Z Haskal, and B V Worgul. Cataract in Interventional Radiology an Occupational Hazard? . *Investigative Ophthalmology and Visual Science*, 45(13):388, 2004.

[23] R E Alvarez and A Macovski. Energy-selective reconstructions in X-ray computerised tomography. *Physics in Medicine and Biology*, 21(5):733, 1976.

[24] M. G. Petrushanskii and E. A. Kornev. On determination of the effective energy of a mixed X-ray beam. *Biomedical Engineering*, 40(2):102–105, 2006.

[25] J H Hubbell and S M Seltzer. Tables of X-Ray mass attenuation coefficients and mass energy-absorption coefficients (version 1.4), 2004.

[26] Thorsten R C Johnson. Dual-energy CT: general principles. *AJR. American journal of roentgenology*, 199(5 Suppl), 2012.

Appendix A

Dosimetry study

Data processing was performed using MATLAB® version R2016B (The MathWorks, Inc., Natick, MA, USA).

Statistical analysis was performed using RStudio version 1.0.153 (RStudio, Inc., Boston, MA, USA).

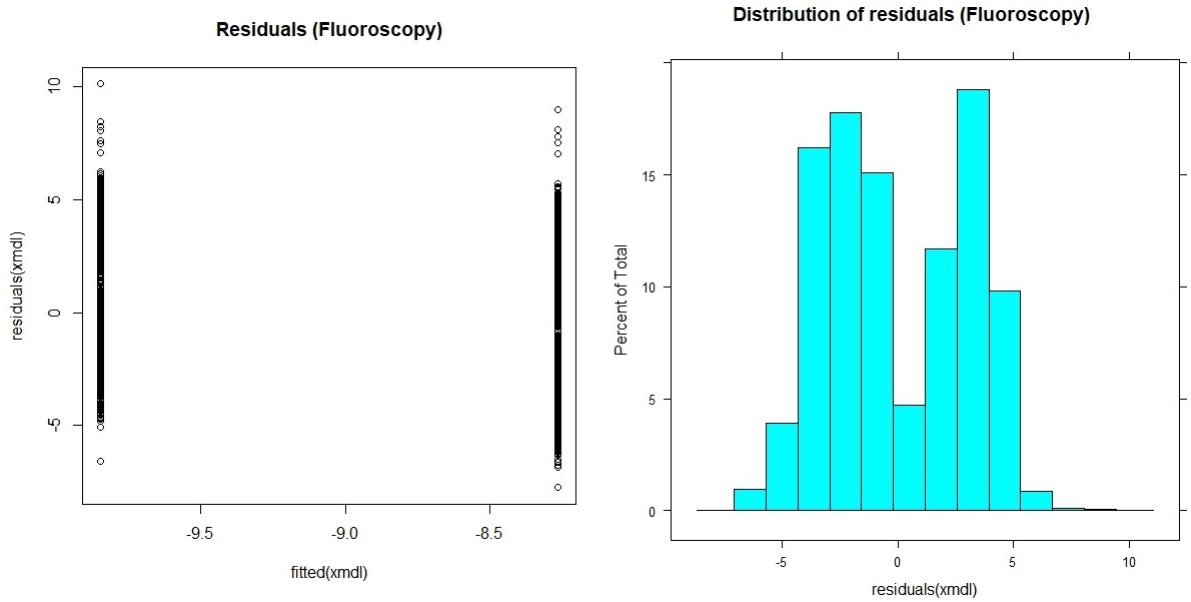

Fig. A.1 Residuals plots for the *per-run* fluoroscopy data subset. **Left:** Residual plot; the two lines correspond with the control and study groups **Right:** Distribution of residuals

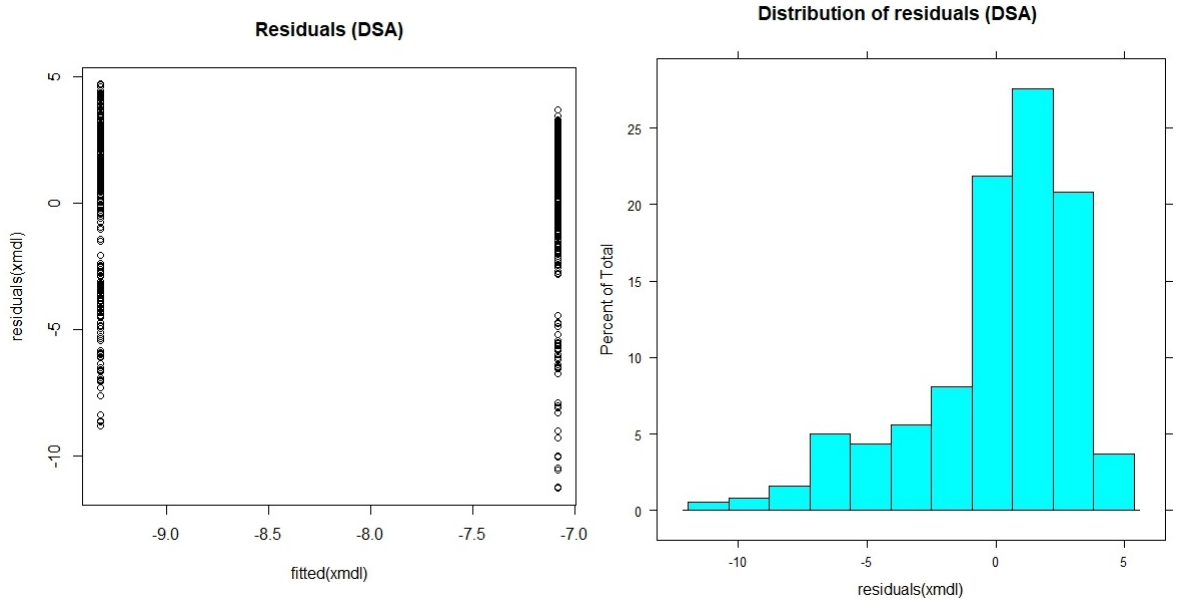

Fig. A.2 Residuals plots for the *per-run* DSA data subset. **Left:** Residual plot; the two lines correspond with the control and study groups **Right:** Distribution of residuals

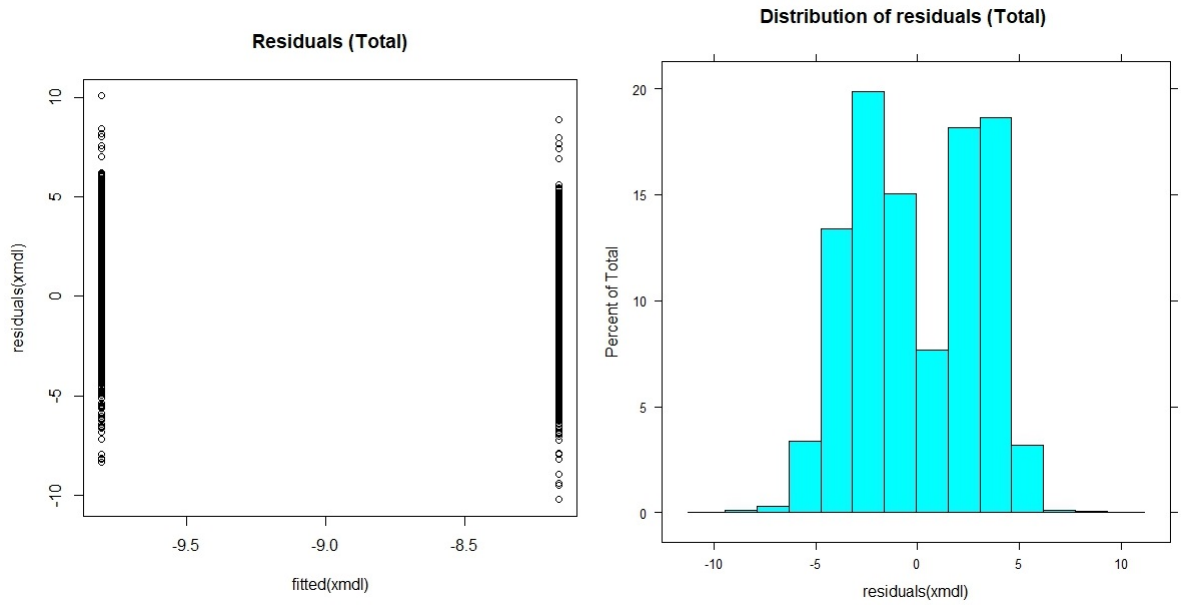

Fig. A.3 Residuals plots for the *per-run* total dataset. **Left:** Residual plot; the two lines correspond with the control and study groupst **Right:** Distribution of residuals

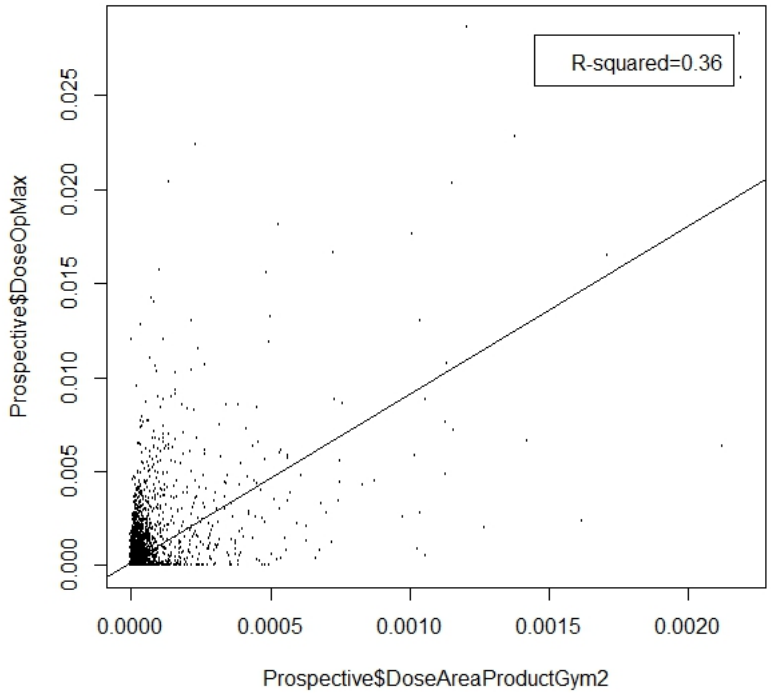

Fig. A.4 Scatterplot of the measured operator dose on the y-axis versus the DAP of the associated imaging run on the x-axis. The regression line was fitted using a linear regresssion model which showed an R-squared value of 0.36